

Singularities in water waves and the Rayleigh–Taylor problem

M. A. FONTELOS^{1†} AND F. DE LA HOZ²

¹Instituto de Ciencias Matemáticas (ICMAT, CSIC-UAM-UCM-UC3M), C/ Serrano 123,
28006 Madrid, Spain

²Departamento de Matemática Aplicada, Escuela Universitaria de Ingeniería Técnica Industrial,
Universidad del País Vasco-Euskal Herriko Unibertsitatea, Plaza de la Casilla 3, 48012 Bilbao, Spain

(Received 11 October 2008; revised 14 October 2009; accepted 14 October 2009)

We describe, by means of asymptotic methods and direct numerical simulation, the structure of singularities developing at the interface between two perfect, inviscid and irrotational fluids of different densities ρ_1 and ρ_2 and under the action of gravity. When the lighter fluid is on top of the heavier fluid, one encounters the water-wave problem for fluids of different densities. In the limit when the density of the lighter fluid is zero, one encounters the classical water-wave problem. Analogously, when the heavier fluid is on top of the lighter fluid, one encounters the Rayleigh–Taylor problem for fluids of different densities, with this being the case when one of the densities is zero for the classical Rayleigh–Taylor problem. We will show that both water-wave and Rayleigh–Taylor problems develop singularities of the Moore-type (singularities in the curvature) when both fluid densities are non-zero. For the classical water-wave problem, we propose and provide evidence of the development of a singularity in the form of a logarithmic spiral, and for the classical Rayleigh–Taylor problem no singularities were found. The regularizing effects of surface tension are also discussed, and estimates of the size and wavelength of the capillary waves, bubbles or blobs that are produced are provided.

1. Introduction

One of the most important problems in hydrodynamics involves the evolution of the interface between two infinite, perfect, incompressible and irrotational fluids in two dimensions and under the action of gravity (see figure 1). Throughout the paper, the following will be assumed: gravity is directed in the downward vertical direction; the density of the lower fluid is ρ_1 ; the density of the upper fluid is ρ_2 . Surface tension force, with surface tension coefficient σ , may also enter into the problem by balancing the jump in pressure across the interface. A simple solution to the problem corresponds to a planar interface with the lower fluid moving at a constant horizontal velocity U_1 and the upper fluid moving with constant horizontal velocity U_2 . If we perturb the planar interface $y=0$ with

$$\eta(x, t) = \varepsilon e^{i(kx - \omega t)}, \quad (1.1)$$

† Email address for correspondence: marco.fontelos@uam.es

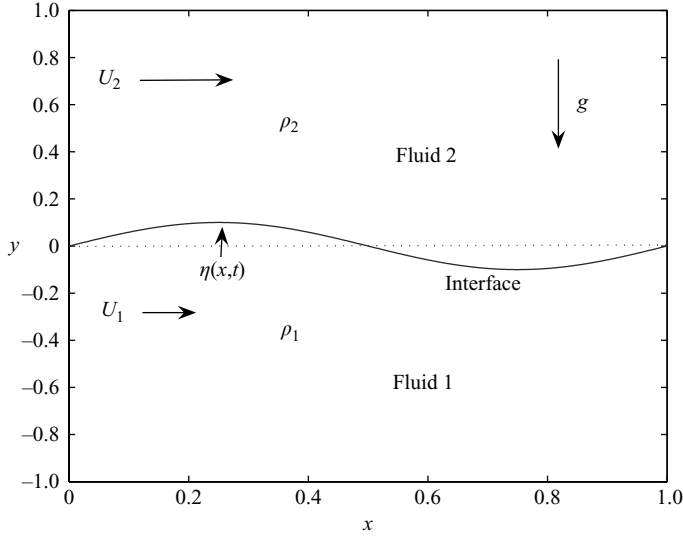


FIGURE 1. Graphical representation of the physical problem.

then it is straightforward to compute the following dispersion relation (see Chandrasekhar 1981, chapters X and XI):

$$\omega = \frac{\rho_1 U_1 + \rho_2 U_2}{\rho_1 + \rho_2} |k| \pm \left[\frac{\rho_1 - \rho_2}{\rho_1 + \rho_2} g |k| + \frac{\sigma}{\rho_1 + \rho_2} |k|^3 - \frac{\rho_1 \rho_2 (U_2 - U_1)^2}{(\rho_1 + \rho_2)^2} k^2 \right]^{1/2}. \quad (1.2)$$

If

$$\Delta = \frac{\rho_1 - \rho_2}{\rho_1 + \rho_2} g |k| + \frac{\sigma}{\rho_1 + \rho_2} |k|^3 - \frac{\rho_1 \rho_2 (U_2 - U_1)^2}{(\rho_1 + \rho_2)^2} k^2 < 0, \quad (1.3)$$

then the small perturbation $\eta(x, t)$ may grow exponentially; i.e. the flat interface becomes unstable. The problem is then to describe the subsequent nonlinear evolution. This problem receives various names depending on the relative densities and velocities of both fluids. By introducing typical length scale L_c , time scale T_c and velocity $U = L_c/T_c$ the dimensionless parameters

$$A_\rho = \frac{\rho_1 - \rho_2}{\rho_1 + \rho_2}, \quad We = \frac{\rho_1 + \rho_2}{2\sigma} U_c^2 L_c, \quad Fr = \frac{U_c}{\sqrt{g L_c}}, \quad (1.4)$$

called the Atwood, Weber and Froude numbers, respectively, can be constructed. Depending on the value of the Atwood number, the particular cases are named as follows:

- $A_\rho = -1, U_1 = U_2 \Rightarrow$ Rayleigh–Taylor instability;
- $A_\rho = 0, U_1 \neq U_2 \Rightarrow$ Helmholtz–Kelvin instability, vortex sheets;
- $A_\rho = 1, U_1 \neq U_2 \Rightarrow$ Thomson instability, water-wave problem.

These cases are named after the scientists that most contributed to their analysis or the physical situation modelled. One can also study water waves when $\rho_2 > 0$ and $0 < A_\rho < 1$ and the Rayleigh–Taylor instability when $\rho_1 > 0$ and $-1 < A_\rho < 0$. We refer to $A_\rho = 1$ and $A_\rho = -1$ as the classical water-wave and Rayleigh–Taylor problems, respectively. These problems can be considered both with and without surface tension, that is for $We < \infty$ and $We = \infty$.

The particular case of the water-wave problem has a special historical importance. Since the early contributions of Laplace, Poisson and Cauchy in the first half of the 19th century aiming to describe the shape and propagation properties of travelling waves, numerous scientists such as Helmholtz, Russell, Stokes, Airy, Thomson and Rayleigh contributed in the second half of the century to the description of various types of waves (progressive, standing, solitary). Thomson showed that the surface of water, under the action of wind, becomes unstable no matter how small its velocity is. If surface tension is included, then a wind-velocity threshold for instability is set. At the same time, Helmholtz initiated the study of vortex sheets with the motivation of understanding the air flow in organ pipes in the mind. Later, Rayleigh studied the instability induced in a fluid with varying density, being the limit of a heavy fluid over a lighter one, a particular case, as well as the instabilities at the interface between two fluids of equal density. We recommend the book by Darrigol (2006) for a thorough historical account. In the 20th century, new mathematical tools were developed in order to study these problems. In the two-dimensional case, complex variable techniques are particularly powerful. The fluids being incompressible and irrotational, the velocity in each fluid can be written as the gradient of a harmonic function. Then it can be written in terms of Cauchy integrals along the interface (we will discuss this in more detail in the next section). In this way, the vortex-sheet problem can be reduced to solving an integro-differential equation, called the Birkhoff–Rott equation, for the complex $z(\alpha, t) = x(\alpha, t) + iy(\alpha, t)$, where (x, y) is the moving interface parameterized by α at time t . Similar equations have been deduced for water waves and the evolution of interfaces for general A_ρ (Baker, Meiron & Orszag 1982; Dyachenko *et al.* 1996). Being of particular importance these formulations are specially suited for numerical implementation (e.g. Hou, Lowengrub & Shelley 1994; Beale, Hou & Lowengrub 1996). Formulations based on complex variable techniques are also part of mathematical proofs of well-posedness for these equations. It turns out that the water-wave problem allows solutions for any sufficiently smooth initial data, at least for a short period of time (Wu 1997; Ambrose & Masmoudi 2005), and has solutions for very long times if the initial data are a small perturbation of a flat interface (Wu 2009).

Of special interest is the mathematical description of fluid patterns that develop during the evolution. In the vortex-sheet problem, the interface may evolve into multiple spirals. In the water-wave problem, waves of multiple types (travelling, solitary, standing) and the phenomenon of wave-breaking (Banner & Peregrine 1993; Sirviente & Song 2004) may take place. In the Rayleigh–Taylor problem, fingers of the heavy fluid entrain the lighter fluid and may destabilize, giving rise to spiral-type patterns. Rayleigh–Taylor instability also occurs when an accelerated fluid displaces another fluid (Taylor 1950), as is the case in stellar explosions.

For these problems, and in the absence of surface tension, it is a well-known fact that singularities may develop in finite time. Since the original work of Moore (1979), the vortex-sheet problem is known to develop curvature singularities (Caflich & Orellana 1989), while the question whether the water-wave problem develops singularities remains open (see, for instance, the review by Craig & Wayne 2007). The Rayleigh–Taylor problem is known not to develop singularities for certain initial data and there is evidence that no singularities develop in general (Clavin, Duchemin & Josserand 2005). Nevertheless, if the density of the lower fluid is non-zero, Rayleigh–Taylor instabilities may still give rise to singularities, as calculations based on a localized approximation (for the singular integrals that appear in the equations) indicate

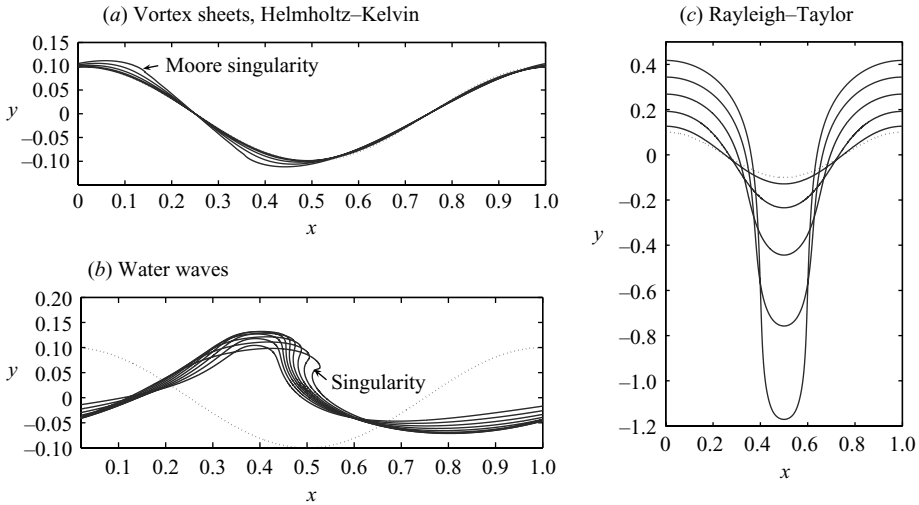


FIGURE 2. Evolution of (a) a vortex sheet, (b) a water wave and (c) an interface undergoing Rayleigh–Taylor instability. The interface at various equally spaced times is represented in each case. Dotted lines correspond to the initial interface profiles. The curves were obtained using the numerical method of this paper.

(Baker, Caffisch & Siegel 1993). See figure 2 for a representation of the solutions of the vortex-sheet, water-wave and Rayleigh–Taylor problems, without surface tension, at various times, based on the numerical results obtained with the method in this paper.

The addition of surface tension or viscous effects may regularize the singularities, but the behaviour of the regularized solution may still be determined by the mathematical structure of the singularities. This is the case, for instance, of the vortex-sheet problem regularized by surface tension (de la Hoz, Fontelos & Vega 2008): Moore singularity is regularized and a spiral pattern starts to emerge. We will see in this paper that the singularities that appear in water waves, in the form of two armed logarithmic spirals, are regularized by surface tension; characteristic capillary wave patterns emerge and a bubble is entrained into the fluid.

For the classical Rayleigh–Taylor instability, $A_\rho = -1$, the addition of surface tension smoothes the tip of the spike of heavy fluid entraining the zero-density fluid. The result is a small blob at the tip of the spike. In the range $-1 < A_\rho < 0$, Moore-type singularities appear in the absence of surface tension. When surface tension is included, Moore singularities are regularized, but filaments of heavy fluid emerge from them and entrain the lighter fluid (see figure 3), which enhances the mixing of both fluids. This fact serves to stress the crucial role that Moore singularities play.

The paper is organized as follows. In §2, we describe the mathematical formulation of the problem as a geometric evolution equation for the interface. In §3, Moore singularities in the range $-1 < A_\rho < 1$ are described. Section 4 is devoted to the water-wave problem, $A_\rho = 1$, and we describe singularities that develop in a self-similar manner and give rise to a logarithmic spiral at the crest of the waves. Finally, §5 discusses the regularizing effects of surface tension for the water-wave and Rayleigh–Taylor problems and the patterns that emerge in the form of capillary waves, bubbles and blobs.

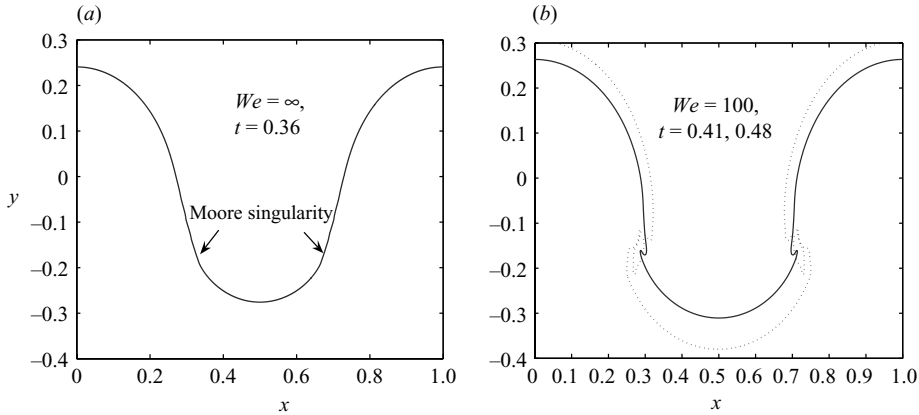


FIGURE 3. (a) Interface profile for $A_\rho = -0.45$ and $We = \infty$ with the development of a Moore curvature singularity at $t = 0.36$. (b) Interface profile for $A_\rho = -0.45$ and $We = \infty$ at time $t = 0.41$ (continuous line) with the development of fingers at the point where Moore singularities were located for $We = \infty$. Profile at time $t = 0.48$ (dotted line) when filamentary structures have grown as well as secondary fingers.

2. Mathematical formulations as geometric evolution and $\theta - L$ equations

In this section, we deduce the mathematical description used in the paper. It is similar to deductions in various publications (cf. Baker *et al.* 1982; Hou *et al.* 1994; Ambrose & Masmoudi 2005) where systems of integro-differential equations restricted to the interface are found, but we will conclude with a system of equations written in terms of arclength, which is a geometrically intrinsic parameterization that will be useful for our analysis.

2.1. Model formulation

We are considering incompressible, irrotational fluids and, therefore, the velocity field \mathbf{w} satisfies

$$\nabla \cdot \mathbf{w} = 0, \quad \nabla \times \mathbf{w} = 0, \quad (2.1)$$

which can be written as

$$\mathbf{w} = \nabla \varphi = \nabla^\perp \psi, \quad (2.2)$$

(with $\nabla^\perp = (\partial_y, -\partial_x)$) where φ and ψ (called the potential and stream functions, respectively) are both harmonic:

$$\Delta \varphi = \Delta \psi = 0. \quad (2.3)$$

If we call φ_i , $i = 1, 2$, the potential φ restricted to the regions occupied by fluids 1 and 2, respectively, then Bernoulli equations will hold at both sides of the interface:

$$\varphi_{i,t} + \frac{1}{2} |\nabla \varphi_i|^2 + \frac{p_i}{\rho_i} + gy = 0, \quad (2.4)$$

(where we use the notation $\varphi_{i,t}$ for the derivative of φ_i with respect to t), as well as jump conditions for the pressure:

$$p_1 - p_2 = \sigma \kappa, \quad (2.5)$$

where σ is the surface tension coefficient and κ is the curvature of the interface. In the absence of surface tension, the condition is $p_1 = p_2$. Finally, a kinematic condition for

the interface has to be imposed: the interface will move following the velocity field. Only the normal component of the velocity will change the geometry of the interface (the tangential component only redistributes the particles along the interface) and, hence

$$v_N = \mathbf{w} \cdot \mathbf{n} \quad (2.6)$$

needs to be imposed, where \mathbf{n} is the vector normal to the interface (and \mathbf{t} is the tangent) and v_N is the velocity with which the interface moves in the normal direction.

A new formulation of the problem can be provided by using complex variables techniques. We write the point in the xy plane as complex numbers $z = x + iy$ and introduce the complex potential

$$\Phi = \varphi + i\psi, \quad (2.7)$$

so that the two components of the velocity (u, v) are given by

$$u - iv = \left(\frac{d\Phi}{dz} \right).$$

Since $\Phi(z)$ is analytic at both sides of the interface C and decays at infinity, it can be written as a Cauchy integral involving an unknown function μ defined on C :

$$\Phi(z) = \frac{1}{2\pi i} \int_C \frac{\mu(z', t) dz'}{z - z'}. \quad (2.8)$$

Then

$$\frac{d\Phi}{dz} = \frac{1}{2\pi i} \int_C \frac{\mu_{z'}(z', t) dz'}{z - z'} = \frac{1}{2\pi i} \int_C \frac{\gamma(\alpha', t) d\alpha'}{z - z(\alpha', t)}, \quad (2.9)$$

where

$$\gamma(\alpha, t) = \mu_\alpha(z(\alpha, t), t). \quad (2.10)$$

Formula (2.9) defines a velocity at the interface that is the principal value of (2.9) plus a tangential component of velocity that has a jump across the interface (see Baker *et al.* 1982). Since the tangential component of velocity does not change the geometry of the interface, we use its arbitrary values, and we define the complex velocity w by

$$w^* = \frac{1}{2\pi i} PV \int_C \frac{\gamma(\alpha', t) d\alpha'}{z - z(\alpha', t)}, \quad (2.11)$$

just as in Baker *et al.* (1982), where $w^* = \text{Re } w - i \text{Im } w$ denotes the complex conjugate of w .

Let us define the velocity and position vectors from the real and imaginary parts of the complex numbers w and z :

$$\mathbf{w} = (\text{Re } w, \text{Im } w), \quad (2.12)$$

$$\mathbf{z} = (\text{Re } z, \text{Im } z) = (x, y). \quad (2.13)$$

We choose as parameter α the Lagrangian variable, which is a label attached to the fluid particles initially and is constant during their motion. In the absence of the surface tension, Baker *et al.* (1982) computed from Bernoulli equations (2.4) the evolution equation for γ :

$$\frac{\partial \gamma}{\partial t} = \frac{\partial}{\partial \alpha} \left(\frac{\lambda \gamma^2}{2 s_\alpha^2} \right) - 2A_\rho \left[\text{Re} \left(z_\alpha \frac{\partial w^*}{\partial t} \right) - \frac{\lambda \gamma}{2} \text{Re} \left(\frac{w_\alpha}{z_\alpha} \right) + \frac{1}{8} \frac{\partial}{\partial \alpha} \left(\frac{\gamma^2}{s_\alpha^2} \right) + g y_\alpha \right], \quad (2.14)$$

where s is the arclength parameter and λ is an arbitrary function associated with the arbitrariness of the tangential velocity at the interface through the relation

$$T = \mathbf{w} \cdot \mathbf{t} + \frac{\lambda\gamma}{2s_\alpha}, \tag{2.15}$$

where T is the tangential velocity of the points of the interface. The points of the interface then move obeying the equation

$$\frac{\partial z(\alpha, t)}{\partial t} = w(\alpha, t) + \frac{\lambda\gamma(\alpha, t)}{2z_\alpha^*(\alpha, t)}. \tag{2.16}$$

We now introduce the tangent vector z_s and write

$$z_s = \frac{z_\alpha}{s_\alpha} = \mathbf{e}^{i\theta}, \tag{2.17}$$

where θ is the inclination angle of the vector tangent to the interface with respect to the x axis, and compute

$$\begin{aligned} z_{\alpha t} &= U_\alpha \mathbf{n} + T_\alpha \mathbf{t} - U\theta_\alpha \mathbf{t} + T\theta_\alpha \mathbf{n}, \\ z_{\alpha t} &= s_\alpha \theta_t \mathbf{n} + s_{\alpha t} \mathbf{t}, \end{aligned}$$

where $U = \mathbf{w} \cdot \mathbf{n}$. Hence.

$$\theta_t = \frac{1}{s_\alpha} (U_\alpha + T\theta_\alpha), \tag{2.18}$$

$$s_{\alpha t} = T_\alpha - U\theta_\alpha, \tag{2.19}$$

and we conclude the system of equations with

$$\frac{\partial \gamma}{\partial t} = \frac{\partial}{\partial \alpha} \left(\frac{\lambda \gamma^2}{2 s_\alpha^2} \right) - 2A_\rho \left[s_\alpha \mathbf{w}_t \cdot \mathbf{t} - \frac{\lambda \gamma}{2s_\alpha} \mathbf{w}_\alpha \cdot \mathbf{t} + \frac{1}{8} \frac{\partial}{\partial \alpha} \left(\frac{\gamma^2}{s_\alpha^2} \right) + g y_\alpha \right], \tag{2.20}$$

$$\frac{\partial \theta}{\partial t} = \frac{1}{s_\alpha} \left(\mathbf{w}_\alpha \cdot \mathbf{n} + \frac{\lambda \gamma}{2s_\alpha} \theta_\alpha \right), \tag{2.21}$$

$$\frac{\partial s_\alpha}{\partial t} = \left(\frac{\lambda \gamma}{2s_\alpha} \right)_\alpha + \mathbf{w}_\alpha \cdot \mathbf{t}. \tag{2.22}$$

The case $\sigma > 0$ in (2.5) leads to an additional term $(2\sigma/(\rho_1 + \rho_2))\kappa_\alpha$ at the right-hand side of (2.20). Introducing typical length scale L_c , time scale T_c and velocity $U_c = L_c/T_c$, rescaling $\mathbf{x} \rightarrow L_c \mathbf{x}$, $t \rightarrow T_c t$, $\mathbf{w} \rightarrow U_c \mathbf{w}$, $\Gamma \rightarrow U_c \Gamma$ and introducing the dimensionless quantities We and Fr (see (1.4)), we arrive from (2.20) at

$$\frac{\partial \gamma}{\partial t} = \frac{\partial}{\partial \alpha} \left(\frac{\lambda \gamma^2}{2 s_\alpha^2} \right) - 2A_\rho \left[s_\alpha \mathbf{w}_t \cdot \mathbf{t} - \frac{\lambda \gamma}{2s_\alpha} \mathbf{w}_\alpha \cdot \mathbf{t} + \frac{1}{8} \frac{\partial}{\partial \alpha} \left(\frac{\gamma^2}{s_\alpha^2} \right) + \frac{1}{Fr^2} y_\alpha \right], \tag{2.23}$$

while (2.21) and (2.22) remain unaltered. If surface tension is included in the problem, then an additional term κ_α/We needs to be added at the right-hand side of (2.23).

The system (2.21)–(2.23) may be further simplified with the introduction of

$$\Gamma = \frac{\gamma}{s_\alpha}, \tag{2.24}$$

$$l = s_\alpha, \tag{2.25}$$

that lead to

$$\frac{\partial \Gamma}{\partial t} = -\Gamma \mathbf{w}_s \cdot \mathbf{t} + \frac{1}{2} \lambda \Gamma \Gamma_s - 2A_\rho \left[\mathbf{w}_t \cdot \mathbf{t} - \frac{\lambda \Gamma}{2} \mathbf{w}_s \cdot \mathbf{t} + \frac{1}{4} \Gamma \Gamma_s + \frac{1}{Fr^2} y_s \right], \quad (2.26)$$

$$\frac{\partial \theta}{\partial t} = \mathbf{w}_s \cdot \mathbf{n} + \frac{\lambda \Gamma}{2} \theta_s, \quad (2.27)$$

$$\frac{\partial l}{\partial t} = l \left(\frac{\lambda \Gamma}{2} \right)_s + l \mathbf{w}_s \cdot \mathbf{t}. \quad (2.28)$$

The derivatives with respect to time are at constant Lagrangian parameter α . We take time derivatives at a constant value of s , then the relation

$$f(\alpha, t) = f(s(\alpha, t), t) \quad (2.29)$$

has to be used and the time derivatives changed accordingly,

$$\frac{\partial f}{\partial t} \rightarrow \frac{\partial f}{\partial t} + s_t \frac{\partial f}{\partial s}, \quad (2.30)$$

so that by introducing

$$\frac{D}{Dt} = \frac{\partial}{\partial t} + \left(s_t - \frac{1}{2} \lambda \Gamma \right) \frac{\partial}{\partial s}, \quad (2.31)$$

we can write (2.26) and (2.27) as

$$\frac{D\Gamma}{Dt} = -\Gamma \mathbf{w}_s \cdot \mathbf{t} - 2A_\rho \left[\frac{D\mathbf{w}}{Dt} \cdot \mathbf{t} + \frac{1}{4} \Gamma \Gamma_s + \frac{1}{Fr^2} y_s \right], \quad (2.32)$$

$$\frac{D\theta}{Dt} = \mathbf{w}_s \cdot \mathbf{n}. \quad (2.33)$$

Note that, introducing $\mu \equiv s_t - (\lambda \Gamma / 2)$, (2.28) takes the form

$$\mu_s = \mathbf{w}_s \cdot \mathbf{t}. \quad (2.34)$$

We will see below that for the singularities studied in this paper, the terms involving μ are small in comparison with the other terms in the equations. Hence, we arrive at the following geometric evolution equations:

$$\frac{\partial \Gamma}{\partial t} + \mu \Gamma_s = -\Gamma \mathbf{w}_s \cdot \mathbf{t} - 2A_\rho \left[\left(\frac{\partial \mathbf{w}}{\partial t} + \mu \mathbf{w}_s \right) \cdot \mathbf{t} + \frac{1}{4} \Gamma \Gamma_s + \frac{1}{Fr^2} y_s \right], \quad (2.35)$$

$$\frac{\partial \theta}{\partial t} + \mu \theta_s = \mathbf{w}_s \cdot \mathbf{n}, \quad (2.36)$$

$$\mu_s = \mathbf{w}_s \cdot \mathbf{t}, \quad (2.37)$$

where

$$\mathbf{w}^*(s, t) = \frac{1}{2\pi i} PV \int \frac{\Gamma(s', t) ds'}{z(s, t) - z(s', t)}, \quad (2.38)$$

and z can be deduced from θ through the relation

$$z_s = e^{i\theta}. \quad (2.39)$$

Equivalent to (2.36) and (2.39), one can write the equation

$$\frac{\partial z}{\partial t} = \mathbf{w}. \quad (2.40)$$

An advantage of the system (2.35)–(2.39) is that it is written in terms of the intrinsic geometric variable s , does not depend on a particular parameterization and carries no ambiguity from a particular choice of tangential velocity. Although the formulation (2.35)–(2.39) is very convenient for analysis, as we will see, it is not simple to implement numerically. A more convenient formulation for numerical purposes is the so-called $\theta - L$ formulation (see Hou *et al.* 1994). If we consider a periodic interface and introduce $L(t)$ as the length of one period, then the variable α defined through

$$s = L(t)\alpha$$

will take values between 0 and 1. Note that $s_{\alpha t} = L_t$ and $(\lambda\gamma/(2s_\alpha)) = T - \mathbf{w} \cdot \mathbf{t}$ so that (2.22) becomes

$$L_t = T_\alpha - U\theta_\alpha, \quad (2.41)$$

and (2.23) and (2.21) become

$$\frac{\partial\gamma}{\partial t} = \left(\frac{(T - \mathbf{w} \cdot \mathbf{t})}{L} \gamma \right)_\alpha - 2A_\rho \left(L\mathbf{w}_t \cdot \mathbf{t} - (T - \mathbf{w} \cdot \mathbf{t})\mathbf{w}_\alpha \cdot \mathbf{t} + \frac{1}{4L^2}\gamma\gamma_\alpha + \frac{1}{Fr^2}\gamma_\alpha \right), \quad (2.42)$$

$$\frac{\partial\theta}{\partial t} = \frac{1}{L} (\mathbf{w}_\alpha \cdot \mathbf{n} + (T - \mathbf{w} \cdot \mathbf{t})\theta_\alpha). \quad (2.43)$$

By periodicity of T , we can compute by integration of (2.41)

$$L_t(t) = - \int_0^1 U\theta_{\alpha'} d\alpha', \quad (2.44)$$

and find T (up to an arbitrary constant) from integration in (2.41).

2.2. Numerical method

Below, we briefly comment on the numerical method used. Equation (2.42) is an integro-differential equation, since it contains \mathbf{w}_t at the right-hand side, which is an integral operator involving γ_t . This causes no concern when $A_\rho = 0$, but needs some rewriting for $A_\rho \neq 0$. Recalling that

$$\mathbf{w}^* = \frac{1}{2\pi i} \int_{-\infty}^{+\infty} \frac{\gamma(\alpha', t)}{z(\alpha, t) - z(\alpha', t)} d\alpha', \quad (2.45)$$

we can compute \mathbf{w}_t^* and decompose it, after integration by parts and use of periodic boundary conditions, in three parts:

$$\begin{aligned} \mathbf{w}_t^* &= \frac{1}{2\pi i} \int_{-\infty}^{+\infty} \frac{\gamma_t(\alpha')}{z(\alpha) - z(\alpha')} d\alpha' - \frac{1}{2\pi i} \int_{-\infty}^{+\infty} \frac{\gamma(\alpha')(z_t(\alpha) - z_t(\alpha'))}{(z(\alpha) - z(\alpha'))^2} d\alpha' \\ &= \frac{1}{2\pi i} \int_{-\infty}^{+\infty} \frac{\gamma_t(\alpha')}{z(\alpha) - z(\alpha')} d\alpha' - \frac{z_t(\alpha)}{2\pi i} \int_{-\infty}^{+\infty} \frac{\gamma(\alpha')}{(z(\alpha) - z(\alpha'))^2} d\alpha' \\ &\quad + \frac{1}{2\pi i} \int_{-\infty}^{+\infty} \frac{\gamma(\alpha')z_t(\alpha')}{(z(\alpha) - z(\alpha'))^2} d\alpha' \end{aligned}$$

$$\begin{aligned}
 &= \frac{1}{2\pi i} \int_{-\infty}^{+\infty} \frac{\gamma_t(\alpha')}{z(\alpha) - z(\alpha')} d\alpha' - \frac{z_t(\alpha)}{2\pi i} \int_{-\infty}^{+\infty} \frac{\gamma(\alpha')}{z_\alpha(\alpha') (z(\alpha) - z(\alpha'))^2} d\alpha' \\
 &\quad + \frac{1}{2\pi i} \int_{-\infty}^{+\infty} \frac{\gamma(\alpha') z_t(\alpha')}{z_\alpha(\alpha') (z(\alpha) - z(\alpha'))^2} d\alpha' \\
 &= \frac{1}{2\pi i} \int_{-\infty}^{+\infty} \frac{\gamma_t(\alpha')}{z(\alpha) - z(\alpha')} d\alpha' + \frac{z_t(\alpha)}{2\pi i} \int_{-\infty}^{+\infty} \left(\frac{\gamma(\alpha')}{z_\alpha(\alpha')} \right)' \frac{d\alpha'}{z(\alpha) - z(\alpha')} \\
 &\quad - \frac{1}{2\pi i} \int_{-\infty}^{+\infty} \left(\frac{\gamma(\alpha') z_t(\alpha')}{z_\alpha(\alpha')} \right)' \frac{d\alpha'}{z(\alpha) - z(\alpha')} \equiv I + II + III, \tag{2.46}
 \end{aligned}$$

where the t dependence and PV notation for the principal value integral have been omitted for the sake of simplicity. Note that z_t can be explicitly computed from z and γ through

$$z_t = U\mathbf{n} + T\mathbf{t} \implies z_t = \frac{1}{L}(iUz_\alpha + Tz_\alpha), \tag{2.47}$$

since U and T involve integral operators depending on z and γ and their space derivatives. It is then immediate to compute II and III in (2.46). The term I involves γ_t , which is also at the left-hand side of (2.42). Hence, using that $\mathbf{w}_t \cdot \mathbf{t} = \text{Re}(\mathbf{w}_t^* z_\alpha)/L$, we can transform (2.42) into

$$\begin{aligned}
 \mathbf{E}(\gamma_t) &\equiv \gamma_t + 2A_\rho \text{Re} \left(\frac{z_\alpha(\alpha)}{2\pi i} \int_{-\infty}^{+\infty} \frac{\gamma_t(\alpha')}{z(\alpha) - z(\alpha')} d\alpha' \right) \\
 &= (\text{Terms involving } z, \gamma \text{ and their space derivatives}), \tag{2.48}
 \end{aligned}$$

where the integral term at the left-hand side of (2.48) can be replaced, for periodic γ and z (with period 1, which is used in this paper), by an integral over one period:

$$\frac{1}{2\pi i} \int_{-\infty}^{+\infty} \frac{\gamma_t(\alpha')}{z(\alpha) - z(\alpha')} d\alpha' = \frac{1}{2i} \int_0^1 \gamma_t(\alpha') \cot(\pi(z(\alpha) - z(\alpha'))) d\alpha'. \tag{2.49}$$

Furthermore, if we view γ_t as a column vector of points $\gamma_t(\alpha_i)$, it is easy to represent numerically the linear operator \mathbf{E} as an $(N \times N)$ matrix:

$$\mathbf{E}(\gamma_t) \equiv \mathbf{E} \cdot \gamma_t. \tag{2.50}$$

Therefore, at a given instant t , the problem of finding γ_t is reduced to solving a system of linear equations. We used an iterational Jacobi–Gauss–Seidel method, with a tolerance in L^∞ -norm equal to 10^{-12} .

Once we have obtained γ_t , it is straightforward to calculate the whole right-hand side of (2.42). The remaining implementational details are the same as described by de la Hoz *et al.* (2008), which were essentially the same as those originally introduced by Hou, Lowengrub and Shelley (1994, 1997).

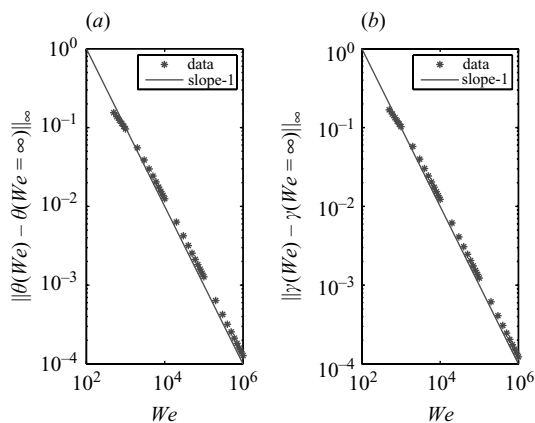
The numerical method also allows surface tension since it only adds κ_α/We into (2.42). For the numerical experiments performed in the next sections, we took as initial data a slightly perturbed interface

$$z(\alpha, 0) = \alpha + 0.1 \cos(2\pi\alpha) \mathbf{i}, \tag{2.51}$$

with a vortex-sheet strength γ :

$$\gamma(\alpha, 0) = -1 + 0.1 \sin(2\pi\alpha), \tag{2.52}$$

N	$\ \theta(N) - \theta(N = 4096)\ _\infty$	$\ \gamma(N) - \gamma(N = 4096)\ _\infty$
64	$1.209512701416660 \times 10^{-2}$	$2.315768139154106 \times 10^{-2}$
128	$1.000863602305557 \times 10^{-3}$	$1.359720107195095 \times 10^{-3}$
256	$3.580713179074380 \times 10^{-6}$	$1.038646570994395 \times 10^{-5}$
512	$1.210555822250825 \times 10^{-10}$	$2.279498811930125 \times 10^{-10}$
1024	$2.129962872743363 \times 10^{-13}$	$4.400924069614121 \times 10^{-13}$
2048	$1.963969473162130 \times 10^{-10}$	$2.211419936060111 \times 10^{-10}$

TABLE 1. Errors of θ and γ at $t = 0.273$ relative to $N = 4096$ for smaller numbers of N .FIGURE 4. Convergence of the evolution variables θ and γ as $We \rightarrow \infty$ to θ and γ of the limiting case $We = \infty$.

for all numerical experiments except for those with $A_\rho = -1$ (classical Rayleigh–Taylor instability), where we take $\gamma(\alpha, 0) = 0$. The value of $1/Fr^2$ is 10 for all numerical computations presented in the following sections.

To validate our numerical method, we have performed the following convergence tests. They are related to the experiment shown in figure 12, with initial data (2.51)–(2.52), at $t = 0.273$.

Given $A_\rho = 1$, $We = \infty$, we have executed the codes for different N , taking $\Delta t = 10^{-4}$; obviously, $\Delta s = 1/N$. In table 1, we have taken as a reference the result for $N = 4096$ at $t = 0.273$, showing that the errors of the evolution variables θ and γ quickly decay in L^∞ -norm, as N is increased, having spectral accuracy in space.

In §5, the effects of finite surface tension are studied. Since the addition of such effects might, in principle, generate capillary waves and make the limit $We \rightarrow \infty$ singular, we have performed a convergence test to show that this is not the case and such a limit is well defined and resolved by our numerical method. In figure 12, a comparison is made between $We = 700$ and $We = \infty$, at $t = 0.273$, suggesting that, as $We \rightarrow \infty$, the interface profiles and vortex strength converge to those of the limiting case $We = \infty$. As evidence, we have executed the codes with $N = 1024$ for a large set of We ranging from $We = 500$ to $We = 10^6$, comparing for each We the evolution variables θ and γ with those of the $We = \infty$ case in L^∞ norm. Power-law convergence, at a rate $\simeq We^{-1}$, to the limiting case is evident from figure 4.

3. Moore singularities for $-1 < A_\rho < 1$

In this section, we describe the structure of the Moore singularities that develop in finite time. Moore singularities are such that both the curvature θ_s and the derivatives of Γ blow up in finite time. Nevertheless, the interface itself has a continuous tangent vector so that we can consider the interface as flat locally near the point at which Moore singularity develops. We can then approximate (see de la Hoz *et al.* 2008, where the same simplification was used and a mathematical estimate of the smallness of the remainder is provided)

$$w^*(s, t) = \frac{1}{2\pi i} PV \int \frac{\Gamma(s', t) ds'}{z(s, t) - z(s', t)} \simeq \frac{1}{2\pi i} \frac{1}{z_s(s, t)} PV \int \frac{\Gamma(s', t) ds'}{s - s'}, \tag{3.1}$$

and then

$$w(s, t) \simeq \frac{1}{2} (H\Gamma) \mathbf{n}, \tag{3.2}$$

where

$$H\Gamma = \frac{1}{\pi} PV \int \frac{\Gamma(s', t) ds'}{s - s'}$$

denotes the Hilbert transform of Γ .

Analogously, after integration by parts using periodicity of Γ and z ,

$$\left. \begin{aligned} w_s^*(s, t) &= -\frac{1}{2\pi i} z_s(s, t) PV \int \frac{\Gamma(s', t) ds'}{(z(s, t) - z(s', t))^2} \\ &= -\frac{1}{2\pi i} z_s(s, t) PV \int \frac{(\Gamma(s', t)/z_{s'}(s', t))_{s'} ds'}{z(s, t) - z(s', t)} \\ &\simeq -\frac{1}{2\pi i} PV \int \frac{(\Gamma(s', t)/z_{s'}(s', t))_{s'} ds'}{s - s'}, \\ w_s(s, t) &\simeq -\frac{1}{2} H(\Gamma\theta_s) \mathbf{t} + \frac{1}{2} (H\Gamma_s) \mathbf{n}, \end{aligned} \right\} \tag{3.3}$$

and

$$\left. \begin{aligned} w_t^*(s, t) &= -\frac{1}{2\pi i} PV \int \frac{(z_t(s, t) - z_t(s', t)) \Gamma(s', t) ds'}{(z(s, t) - z(s', t))^2} \\ &\quad + \frac{1}{2\pi i} PV \int \frac{\Gamma_t(s', t) ds'}{z(s, t) - z(s', t)} \\ &\simeq -\frac{1}{2\pi i} PV \int \frac{z_{st}(s, t) \Gamma(s', t) ds'}{z_s(s, t) z_s(s', t) (s - s')} + \frac{1}{2\pi i} PV \int \frac{\Gamma_t(s', t) ds'}{z_s(s, t) (s - s')}, \\ w_t(s, t) &\simeq -\frac{1}{2} H(\Gamma\theta_t) \mathbf{t} + \frac{1}{2} (H\Gamma_t) \mathbf{n}. \end{aligned} \right\} \tag{3.4}$$

Inserting the approximations (3.2)–(3.4) into (2.35)–(2.37) and neglecting gravity (that represents a subdominant contribution with respect to other terms in the equations that become singular), we get

$$\Gamma_t + \mu\Gamma_s = \frac{1}{2} \Gamma H(\Gamma\theta_s) - 2A_\rho \left[-\frac{1}{2} H(\Gamma\theta_t) - \frac{1}{2} \mu H(\Gamma\theta_s) + \frac{1}{4} \Gamma\Gamma_s \right], \tag{3.5}$$

$$\theta_t + \mu\theta_s = \frac{1}{2} (H\Gamma_s), \tag{3.6}$$

$$\mu_s = -\frac{1}{2} H(\Gamma\theta_s), \tag{3.7}$$

and writing

$$\Gamma = \Gamma_0 + \tilde{\Gamma}, \quad \theta = \theta_0 + \tilde{\theta}, \quad (3.8)$$

with $|\tilde{\Gamma}|, |\tilde{\theta}| \ll 1$ we obtain after integration of the third equation $\mu = -(\Gamma_0 H(\tilde{\theta}))/2$ together with the linearized system

$$\tilde{\Gamma}_t = \frac{1}{2}\Gamma_0^2 H\tilde{\theta}_s - 2A_\rho \left[-\frac{1}{2}\Gamma_0(H\tilde{\theta})_t + \frac{1}{4}\Gamma_0\tilde{\Gamma}_s \right], \quad (3.9)$$

$$\tilde{\theta}_t = \frac{1}{2}(H\tilde{\Gamma}_s). \quad (3.10)$$

Using now the properties

$$H(Hf) = -f, \quad (Hf)_s = Hf_s \quad (3.11)$$

of Hilbert transform in (3.10), we get

$$(H\tilde{\theta})_t = -\frac{1}{2}\tilde{\Gamma}_s, \quad (3.12)$$

and substitution in (3.9) leads to

$$\tilde{\Gamma}_t = \frac{1}{2}\Gamma_0^2 H\tilde{\theta}_s - A_\rho\Gamma_0\tilde{\Gamma}_s, \quad (3.13)$$

which can be combined with (3.12) into the system

$$\begin{pmatrix} \tilde{\Gamma} \\ H\tilde{\theta} \end{pmatrix}_t = \begin{pmatrix} -A_\rho\Gamma_0 & \frac{1}{2}\Gamma_0^2 \\ -\frac{1}{2} & 0 \end{pmatrix} \begin{pmatrix} \tilde{\Gamma} \\ H\tilde{\theta} \end{pmatrix}_s. \quad (3.14)$$

The eigenvalues of the above matrix are

$$\Lambda_\pm = \frac{A_\rho\Gamma_0}{2} \pm \sqrt{1 - A_\rho^2} \frac{\Gamma_0}{2} i, \quad (3.15)$$

which are complex for $|A_\rho| < 1$. This characterizes the system (3.14) as elliptic. Before entering into a more detailed analysis, we remark that the two eigenvalues Λ_\pm are real and identical for $A_\rho = \pm 1$ and the system (3.14) degenerates into the first-order hyperbolic equation

$$\left[\frac{\partial}{\partial t} + \frac{1}{2}\Gamma_0 \frac{\partial}{\partial s} \right] (\tilde{\Gamma} - \Gamma_0 H\tilde{\theta})_t = 0, \quad \text{if } A_\rho = 1, \quad (3.16)$$

$$\left[\frac{\partial}{\partial t} + \frac{1}{2}\Gamma_0 \frac{\partial}{\partial s} \right] (\tilde{\Gamma} + \Gamma_0 H\tilde{\theta})_t = 0, \quad \text{if } A_\rho = -1, \quad (3.17)$$

so that Moore singularities do not take place in these situations and we will have to look for different kind of singularities in the next sections.

Returning to (3.14) for $|A_\rho| < 1$, elementary calculus shows that by introducing

$$s' = \frac{s - \frac{1}{2}A_\rho\Gamma_0 t}{\frac{1}{2}\Gamma_0\sqrt{1 - A_\rho^2}}, \quad (3.18)$$

$$f = \Gamma_0\sqrt{1 - A_\rho^2}\tilde{\Gamma}, \quad (3.19)$$

$$g = A_\rho\Gamma_0\tilde{\Gamma} + H\tilde{\theta}, \quad (3.20)$$

we get

$$\begin{pmatrix} f \\ g \end{pmatrix}_t = \begin{pmatrix} 0 & -1 \\ 1 & 0 \end{pmatrix} \begin{pmatrix} f \\ g \end{pmatrix}_{s'}, \quad (3.21)$$

so that

$$\Delta_{(s',t)} f = \Delta_{(s',t)} g = 0, \quad (3.22)$$

where

$$\Delta_{(s',t)} \equiv \frac{\partial^2}{\partial s'^2} + \frac{\partial^2}{\partial t^2} \quad (3.23)$$

is the Laplace operator.

By taking linear combinations of f and g and Hilbert transform (that commutes with derivatives), we find $\Delta_{(s',t)} \tilde{\theta} = 0$. Taking s derivative (that commutes with s' and t derivatives), we get, for $\kappa = \tilde{\theta}_s$,

$$\Delta_{(s',t)} \kappa = 0. \quad (3.24)$$

Similar to the case of vortex sheets, $A_\rho = 0$, which has been thoroughly studied (see e.g. Moore 1979; Caffisch & Orellana 1989), we can find singular solutions to the curvature in (3.24) in the form

$$\kappa(s', t) = \frac{1}{r^\delta} \sin(\delta\theta + \mu), \quad (3.25)$$

where (r, θ) are the polar coordinates defined as $r = \sqrt{(t - t_0)^2 + (s' - s'_0)^2}$, $\theta = \arctan((s' - s'_0)/(t - t_0))$. Note that (s'_0, t_0) are the space-time of formation of the singularity, $0 < \delta < 1$, $0 < \mu < 2\pi$. Formula (3.25) allows a representation in terms of the self-similar variable $\xi = ((s' - s'_0)/(t - t_0))$ as

$$\kappa(s', t) = \frac{1}{(t_0 - t)^\delta} \frac{1}{(1 + \xi^2)^{\delta/2}} \sin(\delta \arctan \xi + \mu) \equiv \frac{1}{(t_0 - t)^\delta} h(\xi). \quad (3.26)$$

For vortex sheets, $A_\rho = 0$, Moore singularity is known to be such that $\delta = 1/2$, $\mu = 0$. In fact, the local form of the singularity (3.26) coincides with explicit solutions found in Cowley, Baker & Tanveer (1999), who analysed singularities of the problem in the complex spatial plane. We will show below, from numerical simulation, that δ and μ in the Moore singularity that develops at the interface depend on A_ρ . We have simulated the evolution of the interface for A_ρ between 0 and 1 at intervals of 0.05. For all $A_\rho < 1$, we find that the curvature profiles adjust almost perfectly to the functional form (3.26) sufficiently close to the singularity time t_0 for appropriate choices of δ and μ . In figure 5, we show, for $A_\rho = 0.45$, the curvature for various times close to t_0 and the same profiles rescaled with the maximum of the absolute value of the curvature (denoted by $|\kappa_{max}|$) as a function of the rescaled variable ξ . As we can see, they converge to a certain theoretical profile $h(\xi)$ corresponding to certain values of δ and μ . Note that $\delta \simeq 0.97$ and $\mu \neq 0$ (which is clear from the asymmetry of $h(\xi)$), which are values very different from those for vortex sheets. The value of δ may be obtained from the slope of the curve $\log |\kappa_{max}|$ as a function of $\log(t_0 - t)$. As we can see from figure 6, such a slope varies for varying A_ρ . We found that δ increases from 1/2 to almost 1 for A_ρ from zero to approximately 1/2, and then decreases and returns to values close to 1/2 for A_ρ close to 1. The antisymmetry of the self-similar profiles $h(\xi)$ decreases with A_ρ , going from perfectly antisymmetric for vortex sheets to almost symmetric profiles for A_ρ close to 1. In figure 6, we measure the asymmetry with the

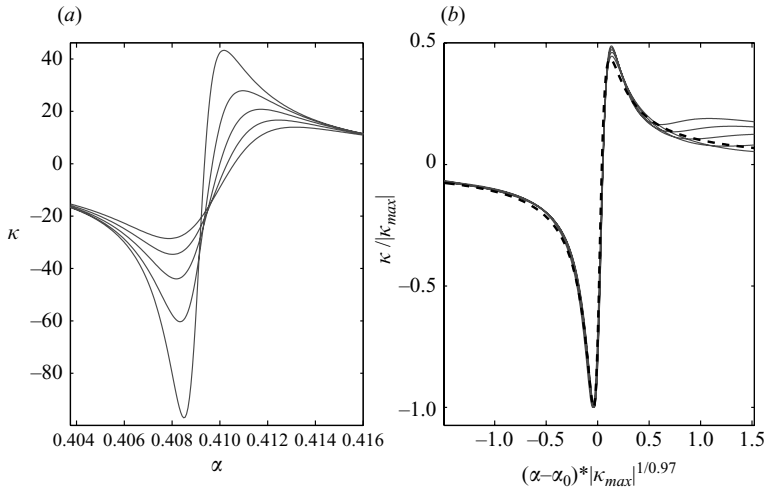


FIGURE 5. (a) Profiles of the curvature for $A_\rho = 0.45$ at various times close to the singularity. (b) The same profiles suitably rescaled together with the theoretical profile (dashed line).

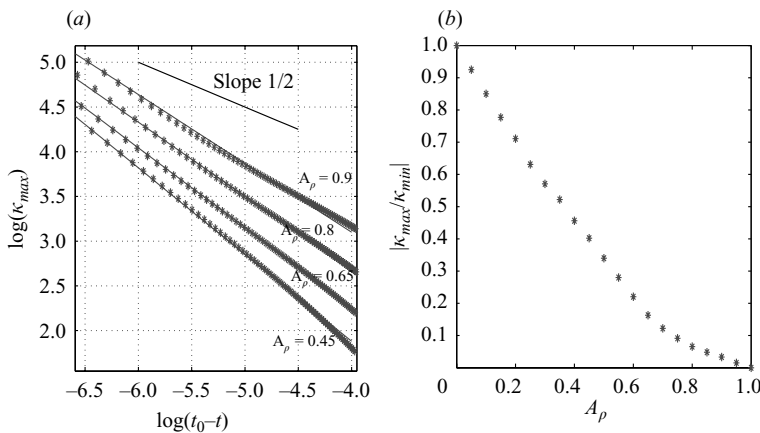


FIGURE 6. (a) Logarithmic plot of the maximum curvature versus time for various A_ρ . (b) Dependence of the absolute value of the ratio between the maximum and minimum curvatures, as t approaches t_0 , as a function of A_ρ .

absolute value of the ratio between the maximum and minimum curvatures. As we can see, it monotonically decreases to zero. The data for $A_\rho = 1$ are an extrapolation since the limit $A_\rho \rightarrow 1$ is singular, and the nature of the singularity is different from the Moore singularity. This singular character is also evident from the values estimated for t_0 for all the A_ρ considered. In all cases with $0 < A_\rho < 0.95$, we found that t_0 is smaller than 0.3. For $A_\rho = 1$, t_0 is well above 0.4 and many of the features of the solution are different.

Moore singularities also develop for $A_\rho < 0$, that is when the heavier fluid is above the lighter fluid. We have seen above that close to a singularity the term involving gravity in (2.35) becomes subdominant with respect to other terms. This implies that the structure of the singularity should be the same for a given $|A_\rho|$ irrespective of the direction of gravity or, equivalently, the relative position of both fluids and hence the

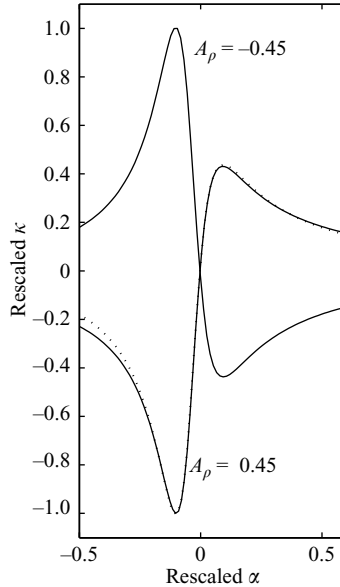


FIGURE 7. Comparison between the self-similar profiles of the curvature for $A_\rho = 0.45$ and $A_\rho = -0.45$. The dashed line shows the mirror image of the $A_\rho = -0.45$ profile.

sign of A_ρ . We have verified this numerically, and, in figure 7, we show the rescaled curvatures close to the time of formation of the singularity for $A_\rho = \pm 0.45$. We can see, aside from a change of sign (due to the different relative positions of heavy and light fluid), the profiles are the same. This implies that both the similarity exponent δ in (3.26) and the degree of asymmetry of the self-similar profile depend on A_ρ . This result contradicts the explicit singular solutions, based on local approximations of the system, found by Baker *et al.* (1993), where the similarity exponent is always $1/2$. Nevertheless, the numerical results of Baker *et al.* (1993) for the complete system without any local approximation are not inconsistent with an A_ρ dependence of the singularity mechanism. The approximation of Baker *et al.* (1993) is based on the assumption that nonlinear interactions between modes with positive and modes with negative wavenumbers can be neglected. This leads to nonlinear systems that can be integrated by means of complex characteristics. The resulting system, when linearized, is equivalent to ours and, hence, it allows a multiplicity of solutions. It is the nonlinear terms, obtained under the assumption that certain nonlinear interactions are negligible, that select a particular generic mechanism. Nevertheless, since the selection does not occur at higher order (the linear systems with multiple singular solutions), but occurs because of lower-order nonlinear interactions, it is important to retain all contributions from the beginning for finding, for a given A_ρ , the particular solution (that is, particular δ and μ) that is selected from the possible solutions in the form (3.26). Unfortunately, we cannot provide yet a mathematical proof of this statement, but only strong numerical evidence. A result of Baker *et al.* (1993) that we also found is the character of $A_\rho = \pm 1$ as singular limits. In the case $A_\rho = -1$ there are no singularities (also found by Clavin *et al.* 2005). In the case of $A_\rho = 1$, there are singularities, but of a different structure and with a singularity time t_0 much larger than any positive $A_\rho < 1$. This case is discussed in §4.

4. Self-similar singularities in classical water waves

The classical water-wave problem assumes that only one fluid has a non-zero density, i.e. $A_\rho = 1$. The equations we have to solve are

$$\frac{D\Gamma}{Dt} = -\Gamma \mathbf{w}_s \cdot \mathbf{t} - 2 \left[\frac{D\mathbf{w}}{Dt} \cdot \mathbf{t} + \frac{1}{4} \Gamma \Gamma_s + \frac{1}{Fr^2} y_s \right], \quad (4.1)$$

$$\frac{D\theta}{Dt} = \mathbf{w}_s \cdot \mathbf{n}. \quad (4.2)$$

Equation (4.1) may be written more compactly in the form

$$\left[\frac{\partial}{\partial t} + \left(\frac{\Gamma}{2} + \mu \right) \frac{\partial}{\partial s} \right] \Gamma + 2 \left[\frac{\partial}{\partial t} + \left(\frac{\Gamma}{2} + \mu \right) \frac{\partial}{\partial s} \right] \mathbf{w} \cdot \mathbf{t} = -2 \frac{1}{Fr^2} y_s, \quad (4.3)$$

or, using

$$\mathbf{w} \cdot \left[\frac{\partial}{\partial t} + \left(\frac{\Gamma}{2} + \mu \right) \frac{\partial}{\partial s} \right] \mathbf{t} = (\mathbf{w} \cdot \mathbf{n}) \left[\frac{\partial}{\partial t} + \left(\frac{\Gamma}{2} + \mu \right) \frac{\partial}{\partial s} \right] \theta,$$

$$\left[\frac{\partial}{\partial t} + \left(\frac{\Gamma}{2} + \mu \right) \frac{\partial}{\partial s} \right] (\Gamma + 2\mathbf{w} \cdot \mathbf{t}) = 2(\mathbf{w} \cdot \mathbf{n}) \left[\frac{\partial}{\partial t} + \left(\frac{\Gamma}{2} + \mu \right) \frac{\partial}{\partial s} \right] \theta - 2 \frac{1}{Fr^2} y_s. \quad (4.4)$$

The first term on the left-hand side of (4.3) is the convective derivative, with velocity $\Gamma/2$, of Γ and hence analogous to the inviscid Burgers equation. The second involves a convective derivative of \mathbf{w} , which is a singular integral operator of Γ and has, therefore, the same scaling properties. We introduce then the self-similar variable

$$\xi = \frac{s}{t_0 - t}, \quad (4.5)$$

analogous to the natural similarity variable in Burgers equation, and seek solutions in the self-similar form

$$\theta(s, t) = \delta \log(t_0 - t) + \Theta(\xi), \quad (4.6)$$

$$\Gamma(s, t) = \Gamma_0 + \Psi(\xi), \quad \mu = \Omega(\xi). \quad (4.7)$$

Consequently,

$$\mathbf{z}(s, t) = (x(s, t), y(s, t)) = (t_0 - t)^{1+i\delta} \mathbf{Z}(\xi) = (t_0 - t)^{1+i\delta} (X(\xi), Y(\xi)), \quad (4.8)$$

$$\mathbf{w}(s, t) = (t_0 - t)^{-i\delta} \mathbf{W}(\xi), \quad (4.9)$$

$$\mathbf{t}(s, t) = (t_0 - t)^{i\delta} \mathbf{T}(\xi), \quad \mathbf{n}(s, t) = (t_0 - t)^{i\delta} \mathbf{N}(\xi). \quad (4.10)$$

Then (4.3) becomes at leading order (with gravity being subdominant) and after simplification

$$\Psi_\xi + 2\mathbf{W}_\xi \cdot \mathbf{T} = 0, \quad (4.11)$$

to be solved together with

$$-\delta + (\xi + \Omega) \Theta_\xi = \mathbf{W}_\xi \cdot \mathbf{N}, \quad (4.12)$$

$$\Omega_\xi - \mathbf{W}_\xi \cdot \mathbf{T} = 0, \quad (4.13)$$

the relation

$$Z_\xi = e^{i\Theta(\xi)}, \quad (4.14)$$

and the following definition of the complex rescaled velocity (whose real and imaginary parts form the components of $\mathbf{W}(\xi)$):

$$W^* = \frac{1}{2\pi i} PV \int_0^\infty \frac{\Psi(\xi') d\xi'}{Z(\xi) - Z(\xi')}. \tag{4.15}$$

Note that from (4.11) and (4.13), it follows $\Omega = -\Psi/2$ and we can write (4.12) as

$$-\delta + (\xi - \Psi/2) \Theta_\xi = \mathbf{W}_\xi \cdot \mathbf{N}, \tag{4.16}$$

so that, if $|\Psi| \ll |\xi|$ for large values of ξ , one can replace (4.12) by

$$-\delta + \xi \Theta_\xi = \mathbf{W}_\xi \cdot \mathbf{N}. \tag{4.17}$$

The homogeneity of (4.11), (4.14), (4.15) and (4.17) suggests the following possible ansatz for a singular solution (representing the asymptotics, for large values of ξ , of self-similar solutions):

$$\Theta(\xi) = \delta \log |\xi| + \beta_\pm, \tag{4.18}$$

$$\Psi(\xi) = v_\pm |\xi|^{\mu_\pm}, \tag{4.19}$$

$$Z(\xi) = e^{i\beta_\pm} \frac{1}{i\delta + 1} |\xi|^{i\delta+1}, \tag{4.20}$$

where the subscript \pm indicates two possibly different values for $\xi > 0$ and $\xi < 0$. From (4.18)–(4.20) one gets, for $\xi > 0$,

$$W^* = \left. \begin{aligned} & \frac{(i\delta + 1)e^{-i\beta_+}}{2\pi i} PV \int_0^\infty \frac{v_+ \xi'^{\mu_+} d\xi'}{\xi^{i\delta+1} - (\xi')^{i\delta+1}} \\ & + \frac{(i\delta + 1)e^{-i\beta_-}}{2\pi i} PV \int_0^\infty \frac{v_- \xi'^{\mu_-} d\xi'}{\xi^{i\delta+1} - e^{(\beta_- - \beta_+)i} (\xi')^{i\delta+1}} \\ & = \xi^{\mu_\pm - i\delta} \left[\frac{(i\delta + 1)e^{-i\beta_+} v_+}{2\pi i} PV \int_0^\infty \frac{\zeta^{\mu_+} d\zeta}{1 - \zeta^{i\delta+1}} \right. \\ & \left. + \frac{(i\delta + 1)e^{-i\beta_-} v_-}{2\pi i} PV \int_0^\infty \frac{\zeta^{\mu_-} d\zeta}{1 - e^{(\beta_- - \beta_+)i} \zeta^{i\delta+1}} \right], \end{aligned} \right\} \tag{4.21}$$

and, therefore,

$$\mathbf{W}_\xi \cdot \mathbf{T} = \text{Re} \{ W_\xi^* Z_\xi \} = |\xi|^{\mu_\pm - 1} \text{Re} \left\{ \frac{(\mu_+ - i\delta)(i\delta + 1)v_+}{2\pi i} PV \int_0^\infty \frac{\zeta^{\mu_+} d\zeta}{1 - \zeta^{i\delta+1}} + \frac{(\mu_- - i\delta)(i\delta + 1)v_-}{2\pi i} PV \int_0^\infty \frac{\zeta^{\mu_-} d\zeta}{1 - e^{(\beta_- - \beta_+)i} \zeta^{i\delta+1}} \right\}, \tag{4.22}$$

$$\mathbf{W}_\xi \cdot \mathbf{N} = \text{Re} \{ iW_\xi^* Z_\xi \} = -|\xi|^{\mu_\pm - 1} \text{Im} \left\{ \frac{(\mu_+ - i\delta)(i\delta + 1)v_+}{2\pi i} PV \int_0^\infty \frac{\zeta^{\mu_+} d\zeta}{1 - \zeta^{i\delta+1}} + \frac{(\mu_- - i\delta)(i\delta + 1)v_-}{2\pi i} PV \int_0^\infty \frac{\zeta^{\mu_-} d\zeta}{1 - e^{(\beta_- - \beta_+)i} \zeta^{i\delta+1}} \right\}. \tag{4.23}$$

For $\xi < 0$, formulae such as (4.22) and (4.23) also hold with β_- and β_+ , as well as v_- and v_+ switched.

Direct substitution into (4.11) and (4.17) yields equations for the coefficients v_\pm , β_\pm , μ_\pm and δ . The invariance of the system under rotations and rescaling of Ψ and Θ reduces the number of free parameters to 5. Instead of seeking an extensive study of the solutions, we will show the existence of, at least, a particular one by

specifying

$$\mu_+ = \mu_- = \mu, \quad v_- = v_+, \quad \beta_- - \beta_+ = \pi, \quad (4.24)$$

which leaves two free parameters in the problem: δ and μ . Since

$$\int_0^\infty \frac{\zeta^\mu d\zeta}{1 - \zeta^{2(i\delta+1)}} = \frac{\pi}{2(i\delta+1)} \cot \frac{\pi(\mu+1)}{2(i\delta+1)} \quad (4.25)$$

(4.11) and (4.17) lead to

$$\mu + \operatorname{Re} \left\{ \frac{\mu - i\delta}{i} \cot \frac{(\mu+1)\pi}{2(i\delta+1)} \right\} = 0, \quad (4.26)$$

$$\operatorname{Im} \left\{ \frac{\mu - i\delta}{i} \cot \frac{(\mu+1)\pi}{2(i\delta+1)} \right\} = 0, \quad (4.27)$$

with solutions that have to be found numerically. One such solution is

$$\delta = -0.298\dots \quad (4.28)$$

$$\mu = 0.540\dots \quad (4.29)$$

It is interesting to study the geometry of the solution we have just constructed. According to (4.8) and (4.20),

$$z(s, t) = e^{i\beta_\pm} \frac{1}{i\delta+1} |s|^{i\delta+1}, \quad (4.30)$$

and, therefore, the polar coordinates are

$$r = |z| = \frac{1}{\sqrt{\delta^2+1}} |s|, \quad (4.31)$$

$$\varphi = \arg z = \beta_\pm + \delta \log |s| - \arctan \delta, \quad (4.32)$$

which implies curves

$$r = \frac{e^{\arctan \delta}}{\sqrt{\delta^2+1}} e^{(\varphi-\beta_\pm)/\delta}, \quad (4.33)$$

which are simply double-armed logarithmic spirals. Such solutions were found by Kambe (1989) in the context of vortex sheets, where the equation to solve is simply the Birkhoff–Rott equation and there is no coupling with any equation for the vortex sheet strength. Next, we show numerically that the solution to the water-wave problem approaches one such double-armed spiral in a self-similar manner. Such a possibility is evidenced in figure 8, where we represent the profile of a breaking wave computed numerically together with logarithmic spirals. The initial data are given in (2.51) and (2.52), periodic boundary conditions are assumed and gravity constant is $1/Fr^2 = 10$. Our numerical simulation is able to reach the stage of formation of a pointed tip at the crest of the wave, but not its winding into the logarithmic spiral (with a radius decreasing exponentially with θ , which poses a huge numerical challenge). In the inset of figure 8, we show a close-up of the double-armed spiral near the tip. Despite these numerical limitations, strong asymptotic arguments based on similarity will be provided below for the formation of spiral patterns.

In figures 9 and 10, we show the curvature κ and vortex strength γ ($= \Gamma_{s_\alpha} = \Gamma L$) for times between 0.419 and 0.459 at intervals of 5×10^{-3} time units. The tendency of the maximum curvature $\kappa_{max}(t) \equiv \max_\alpha |\kappa|$ to blow-up is clear from the figures. In fact, such blow-up occurs at a finite time t_0 as we show below. The

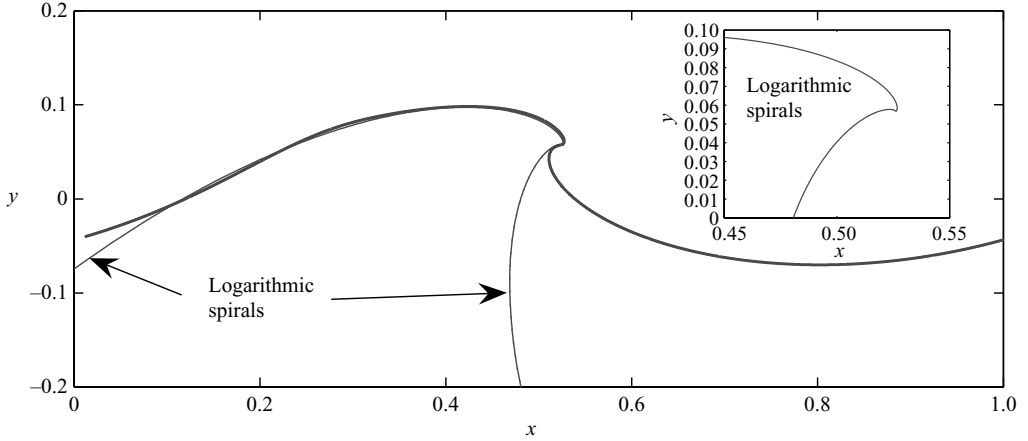


FIGURE 8. Comparison between a breaking wave and a two-armed logarithmic spiral. Inset, detail of the logarithmic spiral close to its centre.

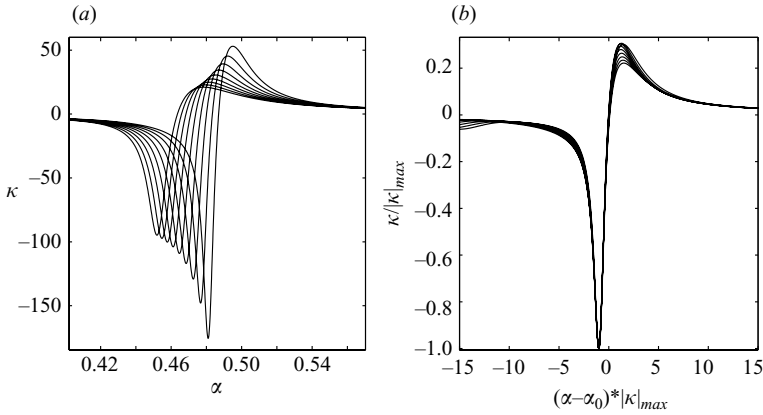


FIGURE 9. (a) Curvature profiles. (b) The same profiles rescaled with the maximum of the absolute value of the curvature.

curvature and vortex strength profiles have similarity properties as illustrated in figures 9(b) and 10(b): by defining

$$\eta \equiv \kappa_{max}(t)(\alpha - \alpha_0(t)), \tag{4.34}$$

we find that the curvature tends to behave as

$$\kappa(\alpha, t) = \kappa_{max}(t)\mathcal{E}(\eta), \tag{4.35}$$

and the vortex strength as

$$\gamma(\alpha, t) = \gamma_{max}(t) + \mathcal{Q}(\eta), \tag{4.36}$$

where $\gamma_{max}(t) \equiv \max_{\alpha} \gamma$. Both $\gamma_{max}(t)$ and $\alpha_0(t)$ are bounded and tend to constants. The same holds for the length of the interface, $L(t)$, in one period, since it only changes about 10% during the whole evolution and tends to some constant L_0 . The functions \mathcal{E} and \mathcal{Q} are universal as evidenced by figures 9(b) and 10(b). The requirement that interface profiles, and hence curvature profiles, remain stationary at a finite α away

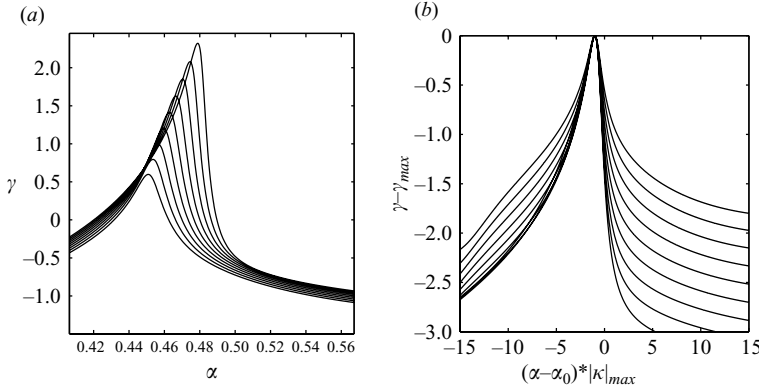


FIGURE 10. (a) Vortex strength profiles. (b) The same profiles with their maximum subtracted and rescaled with maximum of the absolute value of the curvature.

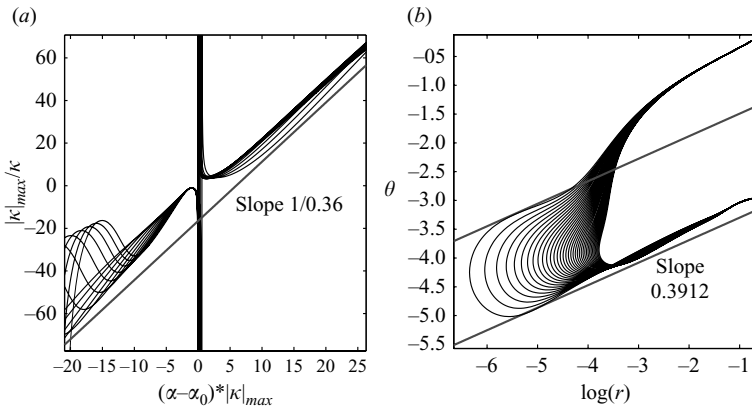


FIGURE 11. (a) Inverse of the rescaled curvature profiles, together with the straight line that best fits their asymptotic behaviour. (b) φ versus $\log r$ for various times close to the t_0 , together with two straight lines representing a two-armed logarithmic spiral in these variables.

from the blow-up point α_0 for t close to t_0 forces the following asymptotics for $\mathcal{E}(\eta)$:

$$\mathcal{E}(\eta) \sim \frac{\tilde{\delta}_{\pm}}{\eta}, \quad \text{as } |\eta| \rightarrow \pm\infty, \quad (4.37)$$

or, introducing the similarity variable $\xi = \kappa_{max}(t)(s - s_0(t)) = L(t)\eta$,

$$\mathcal{E}(\xi) \sim \frac{\delta_{\pm}}{\xi}, \quad \text{as } |\xi| \rightarrow \pm\infty. \quad (4.38)$$

In figure 11(a), we represent the inverse of the rescaled (according to (4.35)) profiles of the curvature together with a straight line of slope 1/0.39. As we can see, the agreement of the asymptotic for the inverse rescaled profiles and the straight line is very good. This would imply that the asymptotics (4.38) are verified with

$$\delta_+ = \delta_- = \delta \simeq 0.39. \quad (4.39)$$

Note that $\theta_s = \kappa$, so that

$$\theta(s, t) = a(t) + \Theta(\xi), \quad (4.40)$$

with $\Theta_\xi(\xi) = \mathcal{E}(\xi)$ and

$$\Theta(\xi) \sim \delta_\pm \log |\xi| + \beta_\pm, \quad \text{as } |\xi| \rightarrow \pm\infty. \quad (4.41)$$

The requirement of stationarity of the interface profiles away from the singularity forces $a(t) = -\delta \log \kappa_{max}(t)$ with $\delta = \delta_+ = \delta_-$. As discussed above, the asymptotics (4.41) represent a double-armed logarithmic spiral. The requirement that the two arms do not intersect also implies $\delta_+ = \delta_-$ as seems to be the case from our numerical experiments.

Analogously, one can write $\Gamma = (\gamma_{max} + \Omega(\eta))/L(t) \simeq \gamma_{max}/L_0 + \Omega(\eta)/L_0 \equiv \Gamma_0 + \Psi(\xi)$. The asymptotics for $\Psi(\xi)$, in view of figure 10(b), are power laws:

$$\Psi(\xi) \sim \nu_\pm |\xi|^{\mu_\pm}, \quad \text{as } |\xi| \rightarrow \pm\infty, \quad (4.42)$$

where the best match (computed by least squares) for the exponents μ_\pm is

$$\mu_- \simeq 0.41, \quad \mu_+ \simeq 0.04. \quad (4.43)$$

The asymptotics in (4.41) and (4.42) match with (4.18) and (4.19) for explicit singular solutions. Hence, our self-similar solution represents the development of a smooth curve whose tip is winding at smaller and smaller length and time scales to develop at t_0 a non-smooth curve that is a double-armed logarithmic spiral. The final profile would be, in polar coordinates positioned at the centre of the spirals,

$$r = A_\pm e^{(\varphi - \beta_\pm)/\delta}, \quad (4.44)$$

for some amplitudes A_\pm . If we represent φ versus $\log r$, then the two spirals (4.44) transform into straight lines of slope δ . In figure 11(b), we show these straight lines together with the numerical profiles, for times between 0.419 and 0.459 at intervals of 10^{-3} time units, in the same coordinates φ and $\log r$.

Our result does not exclude other types of singularities for water waves in contexts different from a breaking wave. This is the case, for instance, of progressive waves of extremal form (Stokes waves) with crests forming an angle of 120° or standing waves also forming singular crests. These singular scenarios are the subject of future research.

5. The effect of surface tension

When adding surface tension, (2.35) has to be replaced by

$$\frac{\partial \Gamma}{\partial t} + \mu \Gamma_s = \frac{1}{We} \theta_{s,s} - \Gamma \mathbf{w}_s \cdot \mathbf{t} - 2A_\rho \left[\left(\frac{\partial \mathbf{w}}{\partial t} + \mu \mathbf{w}_s \right) \cdot \mathbf{t} + \frac{1}{4} \Gamma \Gamma_s + \frac{1}{Fr^2} y_s \right], \quad (5.1)$$

where We and Fr are the Weber and Froude numbers, respectively (see the deduction after (2.22)). The new term $\theta_{s,s}/We$ represents a singular perturbation to (2.35). When the Moore-type singularities develop in the solutions to (2.35) at some time t_0 and space point s_0 , the new term acts as a regularizer and a boundary layer in space and time develops in the neighbourhood of (s_0, t_0) . This analysis was carried out by de la Hoz *et al.* (2008) for the particular case of vortex sheets, $A_\rho = 0$. They found the precise estimate of the size of the arm of the nascent spiral, as $O(We^{-1})$, as well as the velocity with which it develops. Since the analysis for all $|A_\rho| < 1$ is essentially the same, we do not reproduce it here.

In the particular case $A_\rho = 1$, the water-wave problem, the effect of surface tension is known to be different. As we have seen above, a spiral develops already in the case

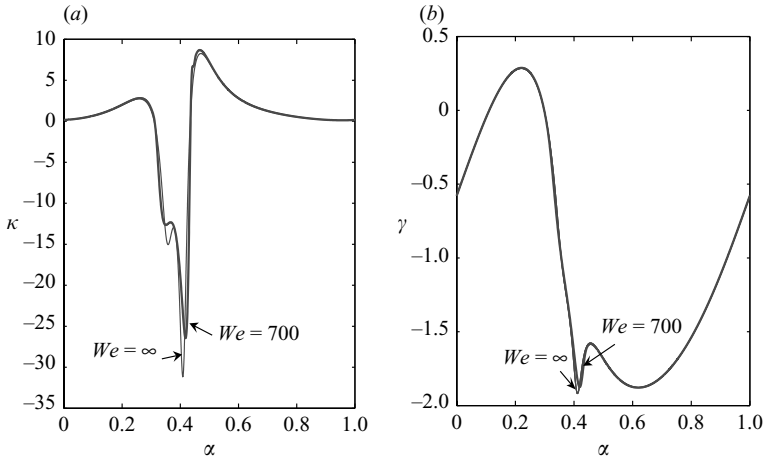


FIGURE 12. Comparison between (a) interface profiles and (b) the vortex strength γ , at $t=0.2730$, for $We=700$ and $We=\infty$.

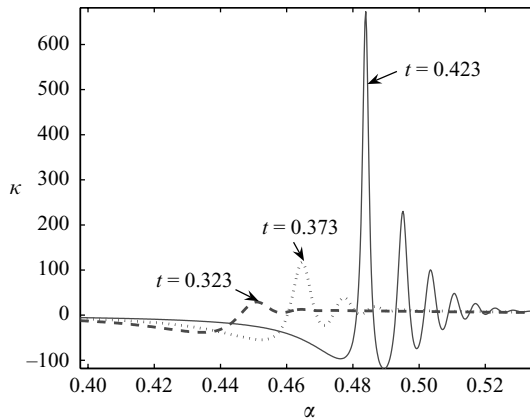


FIGURE 13. Time evolution of the capillary waves that appear for $We=700$.

$We = \infty$, and the role of surface tension is to generate a special form of capillary waves, called Crapper waves (cf. Crapper 1970; Cenicerros & Hou 1999), that eventually may lead to bubble entrainment (cf. Koga 1982). Our goal here is to provide a simple boundary-layer analysis, similar to de la Hoz *et al.* (2008), leading to a quantitative description of Crapper waves and estimate of the entrained bubbles as a function of We .

In figure 12, we show a comparison, for $t=0.2730$, between the profiles of both κ and γ ($=\Gamma/L$) for $We=700$ and $We=\infty$. At this time, the profiles for both values of We are still very similar, but we can see that the minimum of κ does not decrease for $We=700$ as fast as that for $We=\infty$ and the maximum of κ starts to develop an instability in the form of a small oscillation for $We=700$. In figure 13, we show the profiles of κ for later times and one can see that such instability is amplified, convected and keeps its wavelength. Below, we shall estimate the growth rate of these oscillations as a function of Weber number as well as their wavelength. The key

observation to deduce from these results is the fact that the instabilities develop in a small region (that gets smaller with increasing We) around the maximum of the curvature and the vortex strength γ remains approximately constant ($\gamma_0 \simeq -1.5$) there. This allows us to approximate $\Gamma \simeq \Gamma_0 + \tilde{\Gamma}$. We also introduce approximations (3.2)–(3.4) for \mathbf{w} , \mathbf{w}_t and \mathbf{w}_s into the equation for Γ :

$$\left[\frac{\partial}{\partial t} + \left(\frac{\Gamma}{2} + \mu \right) \frac{\partial}{\partial s} \right] \Gamma + 2 \left[\frac{\partial}{\partial t} + \left(\frac{\Gamma}{2} + \mu \right) \frac{\partial}{\partial s} \right] \mathbf{w} \cdot \mathbf{t} = \frac{1}{We} \theta_{ss}, \tag{5.2}$$

and use the smallness of μ to deduce the linear equation

$$\left[\frac{\partial}{\partial t} + \frac{\Gamma_0}{2} \frac{\partial}{\partial s} \right] \tilde{\Gamma} - \Gamma_0 \left[\frac{\partial}{\partial t} + \frac{\Gamma_0}{2} \frac{\partial}{\partial s} \right] H(\theta_s) = \frac{1}{We} \theta_{ss}. \tag{5.3}$$

Equation (4.2) for θ is also approximated by

$$\frac{\partial \theta}{\partial t} = \frac{1}{2} H \tilde{\Gamma}_s. \tag{5.4}$$

By applying the Hilbert transform of (5.4), we obtain $H\theta_t = -\tilde{\Gamma}_s/2$. Then $\tilde{\Gamma}_s = -2H\theta_t$ can be substituted into the s -derivative of (5.3), and we get

$$-2 \left[\frac{\partial}{\partial t} + \frac{\Gamma_0}{2} \frac{\partial}{\partial s} \right]^2 H\theta = \frac{1}{We} \theta_{sss}. \tag{5.5}$$

Applying now the Hilbert transform to (5.5), we conclude with

$$\left[\frac{\partial}{\partial t} + \frac{\Gamma_0}{2} \frac{\partial}{\partial s} \right]^2 \theta = \frac{1}{2We} H\theta_{sss}. \tag{5.6}$$

Finally, we introduce a system of reference moving with velocity $\Gamma_0/2$ by means of the new variables

$$s' = s - \frac{\Gamma_0}{2} t, \quad t' = t \text{ so that } \frac{\partial}{\partial t'} = \frac{\partial}{\partial t} + \frac{\Gamma_0}{2} \frac{\partial}{\partial s}.$$

This leads to

$$\theta_{t't'} = \frac{1}{2We} H\theta_{sss}, \tag{5.7}$$

with elementary solutions

$$\theta(s, t) = e^{\mu t'} \cos(\lambda s), \tag{5.8}$$

provided

$$\mu^2 = \frac{1}{2We} \lambda^3. \tag{5.9}$$

Assuming that, up to multiplicative constants

$$\mu \sim We^\alpha, \quad \lambda \sim We^\beta, \tag{5.10}$$

we obtain, from (5.9),

$$2\alpha = -1 + 3\beta. \tag{5.11}$$

The linearization process carried out above leads to consequences that match almost exactly with our numerical observations. In figure 14, we plot the detail of the profile of breaking waves near the crest for two different values of We . The main observation is that the structures (capillary waves) that appear near the inflection point of the profiles have the same structure but different length scales. In order to estimate the

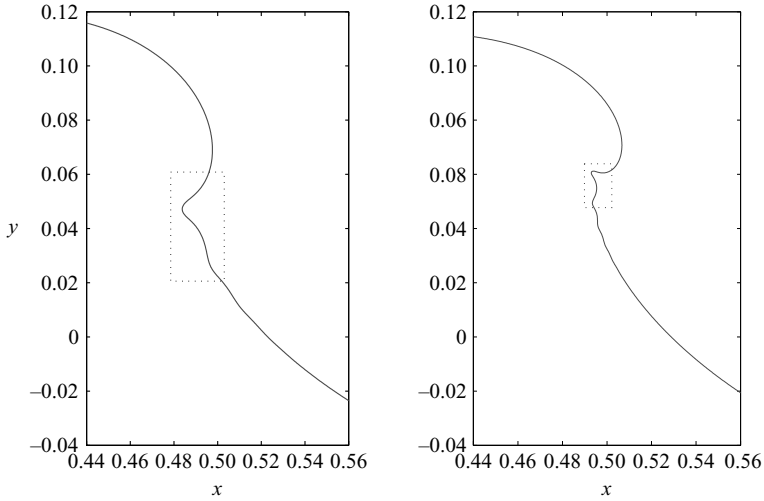


FIGURE 14. The interface profiles near the crest for $We = 200$ (a) and $We = 700$ (b). Inside the dotted boxes we enclose the capillary waves that emerge. In both cases, the shape is the same (up to rotations) but the length scale is different.

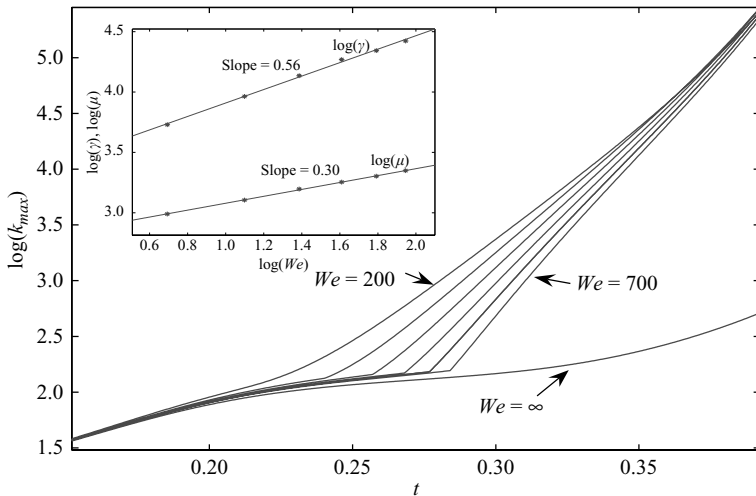


FIGURE 15. Log of the maximum absolute value of the curvature versus time for We between 200 and 700 at intervals of 100. The behaviour tends to be linear as t increases, but with a slope that depends on We . In the inset, we represent, as a function of We , the log of the pre-factor of t in the exponential growth of the capillary waves and the log of their wavenumber, together with linear fits.

wavelength of such capillary waves, we have to estimate λ in (5.8) as a function of We or, more specifically, the exponent β in (5.10). We have simulated the evolution for Weber numbers between 200 and 700, and plotted in figure 15 the logarithm of the maximum curvature versus time. We can see that a linear regime is reached for all $We < \infty$ and we can estimate from it the exponent μ in (5.8) as a function of We . In the inset of figure 15, we represent $\log \mu$ as a function of We and a linear regime with slope of approximately 0.30 appears. This implies $\alpha \simeq 0.30$ in (5.10) and, therefore, from (5.11), $\beta \simeq 0.53$. We estimated the numerical value of β by measuring

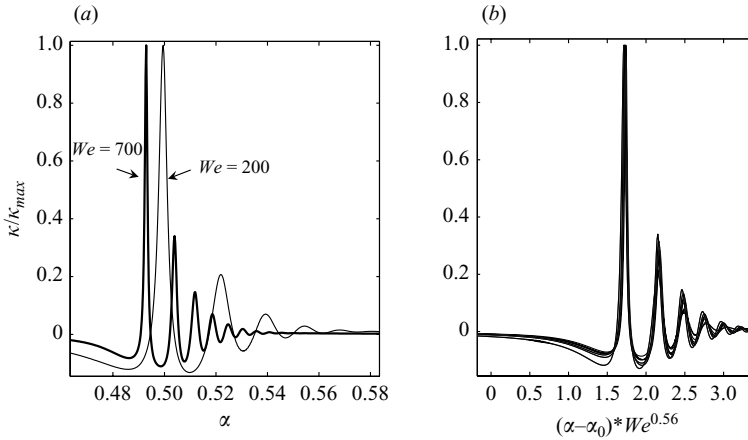


FIGURE 16. (a) The curvature profiles, normalized by the maximum curvature, for $We = 200$ and $We = 700$. (b) The normalized curvature profiles, for We between 200 and 700 at intervals of 100, rescaled according to the power law of We deduced in the text for the wavenumber.

the distance between two consecutive zeros of the propagating waves (i.e. π/λ) for different We . In the inset of figure 15, we represent $\log \lambda$ versus We and we can see a linear regime with slope 0.56, very close to the value $\beta \simeq 0.53$. This estimated accuracy is even more evident in figure 16, where we represent the propagating oscillations for the curvature at a given time, rescaled by the maximum curvature and as a function of a space variable rescaled with $We^{0.56}$. As we can see, the profiles, for We between 200 and 700, rescaled in this way and superposed match almost exactly.

The conclusion of our study on the effects of surface tension in breaking waves is that Crapper waves are created in the neighbourhood of the point of maximum curvature (located at the lower part of the crest) and propagated with velocity $\Gamma_0/2$, together with the crest. These waves have wavelength of size $O(We^{-0.56})$. Their amplitude grows exponentially and this eventually leads to the entrainment of a bubble into the liquid phase. This bubble is also approximately of size $O(We^{-0.56})$.

In the limiting case $A_\rho = -1$, that is the Rayleigh–Taylor instability, no finite-time singularities for $We = \infty$ have ever been found. Arguments based on the analysis of singularities for the problem defined in the spatial complex plane and the impossibility of collapse of such singularities when approaching the physical space support the non-existence of real singularities and the formation, instead, of spikes (Tanveer 1991, 1993). In fact, it was also found numerically by Clavin *et al.* (2005) that the interface develops spikes of the heavy fluid entraining the zero-density fluid. These spikes travel with velocity $\simeq t/Fr^2$ for $t \gg 1$ (i.e. like in free falling), the curvature at the tip of the spike grows with time and is $O(t^3)$ for $t \gg 1$. The tip itself evolves in a self-similar manner: if we fix a system of coordinates (x, y) at the tip, with y being the coordinate in the direction of the spike, then $x = O(t^{-1})$ and $y = O(t)$ or, in other words, we can write the tip as $y = tf(xt)$ with $f(\eta)$ a universal function.

The effect of surface tension, in this case, is to limit the growth of the curvature and keep the tip's curvature below a maximum value that we estimated numerically to be $\simeq O(We^{0.23})$. We show in figure 17(a) the evolution of the tip's curvature (which is also the maximum curvature) as a function of time for various We , together with the maximum curvature reached during the evolution as a function of We and a fit to the power-law $We^{0.23}$. In figure 17(b), we superpose the profiles near the tip for $We = 50$

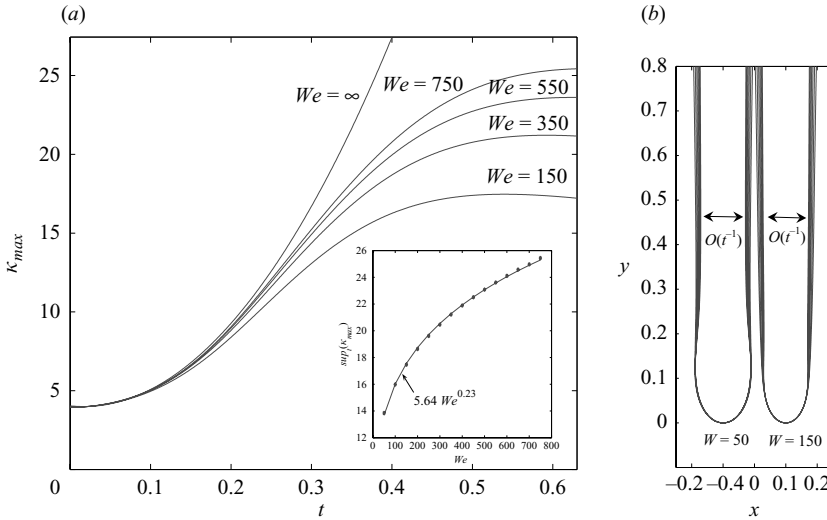


FIGURE 17. (a) Evolution of the maximum curvature with time for various We . In the inset, the maximum curvature reached during the evolution as a function of We , together with a fit to a power law. (b) Superposed interface profiles at various times for $We = 50$ and $We = 150$.

and $We = 150$. For a given We , the tip tends to converge towards a blob of constant size and is connected to the neck of thickness $O(t^{-1})$ (the thickness obtained in the theory for $We = \infty$). The shape and size of the blob depend on We and, since the tip's curvature is $\simeq O(We^{0.23})$, the blob's radius should be $O(We^{-0.23})$. Hence, the effect of surface tension on the Rayleigh–Taylor instability is to produce a rounded blob at the end of the free-falling spike and connected to it by a neck of thickness $O(t^{-1})$. The rigorous analysis of these numerical observations and the study of the blob's shape as a function of We are interesting problems that deserve further investigation.

6. Conclusions

In this article, we have studied the formation (or not) of singularities in various classical problems involving the evolution of the interface between two inviscid and irrotational fluids with different densities. The problem has been considered both with and without surface tension.

Without surface tension and depending on the Atwood ratio A_ρ , we have found singularities developing in finite time when $|A_\rho| < 1$. These are curvature singularities, but with a degree of differentiability that changes as a function of $|A_\rho|$. Explicit expressions for the singularities in terms of similarity variables have been obtained; they form a two-parameter family with the classical Moore singularity as a particular case when $A_\rho = 0$. The limit $A_\rho = 1$, corresponding to classical water waves, is clearly singular. Moore-type singularities cannot take place in this limit and, therefore, solutions can be continued for longer times. Nevertheless, at some later time, the surface revolves over itself and curvature grows very fast, indicating the possible formation of a new kind of singularity. We have described a mechanism for the formation of such a singularity, consisting in the development of a double-armed logarithmic spiral in a self-similar manner, and provided numerical evidence indicating that this might indeed be the kind of singularity that develops in water waves. In

the limit $A_\rho = -1$, no singularities have been found. Instead, we find the growth of a spike, a fact already reported in the literature.

When finite surface tension is included, the Moore singularities are regularized (although a different kind of singularity in the form of self-intersection of the interface may develop later on) and, depending on A_ρ , the effect of surface tension is the appearance of structures in the form of capillary waves, bubbles or blobs. When writing the equations in terms of Weber number, the typical length and time scales for the development of such structures can be estimated in the form of power laws of We . For this analysis, knowledge on the form of the singularities or spikes in the limit $We \rightarrow \infty$ is crucial. The scaling laws have also been verified numerically. The generation of bubbles and estimation of their typical size may be relevant in measurements of gas transfer in breaking waves that have recently been carried out (Tsoukala & Moutzouris 2008).

Various other effects and their impact in singularity formation, besides surface tension, deserve future exploration, in particular, effects of surface tension gradients (due to the presence of surfactants, for instance; Joo, Messiter & Schultz 1991), weak dissipative effects due to finite fluid viscosity (Wang & Baker 2009) or wave interactions due to the presence of solid walls.

This work was initiated while the authors were participating in the program ‘Singularities in Mechanics’ at the Institute Henri Poincaré. The authors thank the hospitality and the optimum scientific environment they enjoyed. We also wish to thank Paul Clavin, Jens Eggers, Christophe Josserand, Luis Vega and Sijue Wu for the very interesting and fruitful conversations held around the general subject of singularities and, in particular, on the subject of the present paper, during the program and afterwards. We also thank Hector D. Cenicerros for valuable suggestions concerning the implementation of the codes used in this paper. The computer simulations were done at Odisea supercomputer facilities from CSIC/UAM. We have been supported by grant MTM2008-0325.

REFERENCES

- AMBROSE, D. M. & MASMOUDI, N. 2005 The zero surface tension limit of two-dimensional water waves. *Comm. Pure Appl. Math.* **58**, 1287–1315.
- BAKER, G., CAFLISCH, R. E. & SIEGEL, M. 1993 Singularity formation during Rayleigh–Taylor instability. *J. Fluid Mech.* **252**, 51–78.
- BAKER, G. R., MEIRON, D. I. & ORSZAG, S. A. 1982 Generalized vortex methods for free-surface flow problems. *J. Fluid Mech.* **123**, 477–501.
- BANNER, M. L. & PEREGRINE, D. H. 1993 Wave breaking in deep water. *Annu. Rev. Fluid Mech.* **25**, 373.
- BEALE, J. T., HOU, T. Y. & LOWENGRUB, J. 1996 Convergence of a boundary-integral method for water waves. *SIAM J. Numer. Anal.* **33** (5), 1797–1843.
- CAFLISCH, R. E. & ORELLANA, O. F. 1989 Singular solutions and ill-posedness for the evolution of vortex sheets. *SIAM J. Math. Anal.* **20** (2), 293–307.
- CENICEROS, H. D. & HOU, T. Y. 1999 Dynamic generation of capillary waves. *Phys. Fluids* **11** (5), 1042–1050.
- CHANDRASEKHAR, S. 1981 *Hydrodynamic and Hydromagnetic Stability*. Dover.
- CLAVIN, P., DUCHEMIN, L. & JOSSERAND, C. 2005 Asymptotic behaviour of the Rayleigh–Taylor instability. *Phys. Rev. Lett.* **94** (22), 224501.
- COWLEY, S. J., BAKER, G. R. & TANVEER, S. 1999 On the formation of Moore curvature singularities in vortex sheets. *J. Fluid Mech.* **378**, 233–267.
- CRAIG, W. & WAYNE, C. E. 2007 Mathematical aspects of surface water waves. *Russ. Math. Surv.* **62**, 453–473.

- CRAPPER, G. D. 1970 Non-linear capillary waves generated by steep gravity waves. *J. Fluid Mech.* **40**, 149.
- DARRIGOL, O. 2006 *Worlds of Flow: A History of Hydrodynamics from the Bernoullis to Prandtl*. Oxford University Press.
- DYACHENKO, A. I., KUZNETSOV, E. A., SPECTOR, M. D. & ZAKHAROV, V. E. 1996 Analytical description of the free surface dynamics of an ideal fluid (canonical formalism and conformal mapping). *Phys. Lett. A* **221**, 73–79.
- HOU, T. Y., LOWENGRUB, J. S. & SHELLEY, M. J. 1994 Removing the stiffness from interfacial flow with surface-tension. *J. Comput. Phys.* **114** (2), 312–338.
- HOU, T. Y., LOWENGRUB, J. S. & SHELLEY, M. J. 1997 The long-time motion of vortex sheets with surface tension. *Phys. Fluids* **9** (7), 1933–1954.
- DE LA HOZ, F., FONTELOS, M. A. & VEGA, L. 2008 The effect of surface tension on the Moore singularity of vortex sheet dynamics. *J. Nonlinear Sci.* **18**, 463–484.
- JOO, S. W., MESSITER, A. F. & SCHULTZ, W. W. 1991 Evolution of weakly nonlinear water waves in the presence of viscosity and surfactant. *J. Fluid Mech.* **229**, 135–158.
- KAMBE, T. 1989 Spiral vortex solution of Birkhoff–Rott equation. *Physica D* **37**, 463–473.
- KOGA, M. 1982 Bubble entrainment in breaking wind waves. *Tellus* **34**, 481.
- MOORE, D. W. 1979 Spontaneous appearance of a singularity in the shape of an evolving vortex sheet. *Proc. R. Soc. Lond. A* **365**, 105–119.
- SIRVIENTE, A. I. & SONG, C. 2004 A numerical study of breaking waves. *Phys. Fluids* **16** (7), 2649–2667.
- TANVEER, S. 1991 Singularities in water waves and Rayleigh–Taylor instability. *Proc. R. Soc. Lond. A* **435**, 137–158.
- TANVEER, S. 1993 Singularities in the classical Rayleigh–Taylor flow: formation and subsequent motion. *Proc. R. Soc. Lond. A* **441**, 501–525.
- TAYLOR, G. I. 1950 The instability of liquid surfaces when accelerated in a direction perpendicular to their planes. I. *Proc. R. Soc. Lond. A* **201**, 192–196.
- TSOUKALA, V. K. & MOUTZOURIS, C. I. 2008 Gas transfer under breaking waves: experiments and an improved vorticity-based model. *Ann. Geophys.* **26**, 2131–2142.
- WANG, J. & BAKER, G. 2009 A numerical algorithm for viscous incompressible interfacial flows. *J. Comput. Phys.* **228** (15), 5470–5489.
- WU, S. 1997 Well-posedness in Sobolev spaces of the full water wave problem in two-dimensional. *Invent. Math.* **130** (1), 39–72.
- WU, S. 2009 Almost global wellposedness of the two-dimensional full water wave problem. *Invent. Math.* **177** (1), 45–135.